A Wideband Low-RCS Metasurface-Inspired Circularly Polarized Slot Array Based on AI-Driven Antenna Design Optimization Algorithm

Qi Zheng, Chenjiang Guo, Jun Ding, Mobayode O. Akinsolu, Bo Liu, and Guy A. E. Vandenbosch

***Abstract*—A metasurface-inspired low-profile circularly polarized (CP) slot array with a wide CP band and broadband low radar cross section (RCS) is proposed in this paper. The slot array consists of four element antennas, four grounded substrates, and a sequential-rotated feeding network. In terms of radiation performance, the array yields a wide CP band resulting from the CP element antenna and the sequential-rotated feeding network. The CP element antenna is achieved due to the polarization conversion property of the metasurface-based superstrate. The feeding network with multiple related design parameters is optimized by an AI-driven antenna design method to find the widest bandwidth. In terms of scattering performance, broadband RCS reduction is achieved by using a hybrid RCS reduction technique that combines two destructive interference principles. The $|S_{11}|$<-10 dB bandwidth reaches 53.2%, the AR < 3 dB bandwidth reaches 50%, and the RCS reduction bandwidth reaches 147.8% for a low-profile structure with a relatively low number of metasurface unit cells. A prototype was fabricated and measured. The measured and simulated results are in good agreement.**

***Index Terms*—Metasurface (MS), circular polarization, radar cross section (RCS), antenna array, parallel surrogate model-assisted hybrid differential evolution for antenna optimization (PSADEA)**

I. INTRODUCTION

In the last few decades, radar cross section (RCS) [1] associated with the stealth capability of a target has attracted a lot of interest. Antennas which are widely used in many devices to transmit and receive signals can also function as special scatters. Amongst them, the array antenna, which has a large aperture, makes a tremendous contribution to the overall RCS of a platform. Many methods such as structural shaping, and using radar absorbing material and frequency selective surfaces (FSS) have been studied to reduce the RCS of antennas [2-6]. These methods are mainly based on energy deflection or energy dissipation and their drawbacks include narrow bandwidth and deterioration of radiation performance.

Manuscript received xx,xx. This work was supported in part by Natural Science Foundation of Shanghai (No.21ZR1424300) and China Scholarship Council (No. 201806290108) (Corresponding authors: Qi Zheng (design), Guy A. E. Vandenbosch (design) and Bo Liu (algorithm)).

Q. Zheng is with the School of Communication and Information Engineering, Shanghai University, Shanghai, China(e-mail: qizheng@shu.edu.cn).

C. Guo, and J. Ding are with the School of Electronics and Information, Northwestern Polytechnical University, Xi'an China. (e-mail: cjguo@nwpu.edu.cn, dingjun@nwpu.edu.cn).

M. O. Akinsolu is with the Faculty of Arts, Science and Technology, Wrexham Glyndwr University, Wrexham U.K. LL11 2AW. (e-mail: m.o.akinsolu@ieee.org)

B. Liu is with James Watt School of Engineering, University of Glasgow, Glasgow, Scotland. G12 8QQ. (e-mail: bo.liu@glasgow.ac.uk)

G. A. E. Vandenbosch is with the ESAT-WaveCoRE Research Division, Department of Electrical Engineering, KU Leuven, 3001 Leuven, Belgium. (e-mail: guy.vandenbosch@kuleuven.be).

Color versions of one or more of the figures in this communication are available online at http://ieeexplore.ieee.org.

Digital Object Identifier 10.1109/TAP.2016.xxx

In recent years, metamaterials (MTMs), particularly, artificially constructed periodical structures, have been demonstrated to be effective in both RCS reduction and low-RCS antenna design. Checkerboard patterned configurations using artificial magnetic conductors (AMC) [7], electromagnetic bandgap structures (EBG) [8], and polarization rotation reflective surfaces [9] are some examples of MTM-based approaches which have provided new techniques for RCS reduction. These techniques are mostly based on reflection tuning, a method that can also be employed in the design of low-RCS antennas [10-13]. New low-RCS CP array antennas with few MS unit cells designed by using an MS and grounded substrate have also been proposed based on the checkerboard configuration, yielding $180° \pm 30°$ reflection phase difference between adjacent components [14], [15]. The alternative technique of using polarization conversion metamaterials with checkerboard configuration has also been widely employed in the design of low-RCS antennas [16-19]. For this technique, the RCS reduction results from the anti-phase of the cross-polarized components of the reflected fields of adjacent sections. This technique has also been combined with Fabry-Perot (F-P) antennas for CP radiation and with linearly polarized (LP) source antennas for low RCS [20].

Although several low-RCS antennas and arrays have been proposed, the challenges of achieving wideband RCS reduction as well as wideband CP radiation remain. In this paper, an MS-inspired low-profile wideband low-RCS CP array is proposed. The contributions are as follows:

1) The array achieves a broadband RCS reduction as well as a wide CP band by using an MS-based superstrate. The broadband RCS reduction of the array is achieved through the combination of two different destructive interference mechanisms with a relatively low number of MS unit cells. The wide CP band obtained is attributed to the CP element antenna and sequential-rotated feeding network.

2) The array achieves the widest CP band compared to other low RCS arrays in literature. The CP is achieved at the element level with the MS-based superstrate's conversion of the LP electromagnetic wave radiating from the slot antenna into a CP wave. An AI-driven antenna design algorithm is employed to obtain optimal performance.

The sequentially rotated feeding network, which is generally associated with multiple related design parameters, is a challenge in CP array design [21]. To obtain the desired wideband CP slot array, optimization of the proposed structure is essential. Optimizers available in CST Microwave Studio were firstly employed, but all failed to obtain acceptable designs. Hence, the parallel surrogate model-assisted hybrid differential evolution for antenna optimization (PSADEA) method [23][24] was then employed. PSADEA is a state-of-the-art machine learning-assisted antenna design optimization method, belonging to the SADEA series [23]-[27]. The SADEA series employs the Gaussian process to build surrogate models predicting antenna performances, differential evolution to carry out global optimization, and a surrogate model-aware evolutionary search framework to harmonize surrogate modeling and optimization.

In the SADEA series, PSADEA particularly selects a certain set of complementary DE mutation operators and controls their usage

through reinforcement learning. The surrogate modeling scheme was also adapted to match the new search scheme. Due to this, PSADEA can address challenging design cases with very stringent antenna design specifications, for which, standard global optimization algorithms (e.g., particle swarm optimization) may not be able to address successfully. PSADEA also shows optimization efficiency improvement by up to 20 times compared to several popular global optimization methods [23] [24]. PSADEA has been used to address many challenging antenna problems such as [28] [29], and in this paper, it is applied to the proposed CP slot array.

The remainder of the paper is organized as follows: Section II describes the proposed array, including the design of the element antenna and the mechanism of broadband RCS reduction. Section III presents and discusses the experimental results. Concluding remarks are provided in Section IV.

II. Low-RCS Circularly Polarized Slot Array

A. Topology of the array

Fig. 1 shows the topology of the array. As shown in Fig. 1(a), the h_2 - thick dielectric top superstrate contains the printed MSs. As shown in Figs. 1(b) and (c), at the bottom of a dielectric substrate with a thickness of h_1, there is a sequential rotated feeding network exciting four orthogonal slots in a metallic ground. The feeding network is based on a series-parallel strip with a curved structure [21]. The quarter-wavelength impedance transformers with Z_i (i=1, 2, …, and 8) were designed to provide the necessary impedance matching and 90° output phase delays. The optimized parameters of the feeding network using the PSADEA method are given in Table I. The optimized impedances are (100.8 Ω, 57.66 Ω, 100.80 Ω, 79.33 Ω, 45.93 Ω, 141.68 Ω, and 70.59 Ω)

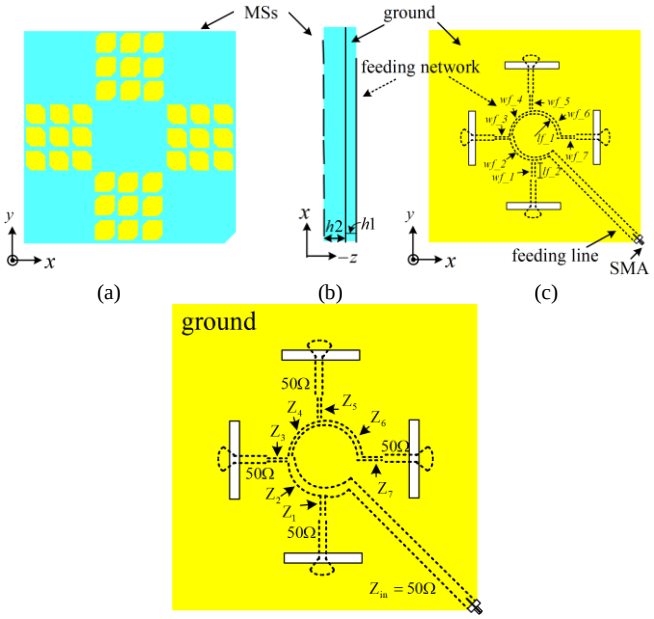

Fig. 1 Schematic diagram of the array.

B. Mechanism of circular polarization

Each element antenna consists of an MS-based superstrate integrated with a traditional LP slot antenna. Fig. 2 shows the layout of an element of the array. The superstrate consists of 3×3 unit cells printed on a substrate having relative permittivity (ε_r) of 3.5, loss tangent ($\tan\sigma$) of 0.0026, and a thickness of 3 mm. The MS unit cell is a square patch with two triangularly truncated corners. The structure is modeled and discretized for simulations using CST Microwave Studio. The geometric parameters are $p=10$ mm, $a=9.5$ mm, $b=3.5$ mm, $ls=20$ mm, $ws=2.2$ mm, $\theta_f=45°$, $rf=7$ mm, $wf=1.2$ mm, $h1$=3 mm, $h2=0.5$ mm, and $L=30$ mm.

TABLE I
Parameters for the Design Exploration of the Proposed Array

Parameters	Design 1	
	Range	PSADEA-Optimized Value
wf_1	0.3 mm – 0.5 mm	0.28 mm
wf_2	0.7 mm – 1.1 mm	0.90 mm
wf_3	0.2 mm – 0.4 mm	0.28 mm
wf_4	0.4 mm – 0.8 mm	0.49 mm
wf_5	0.7 mm – 1.5 mm	1.30 mm
wf_6	0.1 mm – 0.6 mm	0.10 mm
wf_7	0.6 mm – 1 mm	0.62 mm
lf_1	5 mm – 7 mm	5.70 mm
lf_2	7 mm – 11 mm	8.99 mm
rf	4 mm – 8 mm	7.82 mm

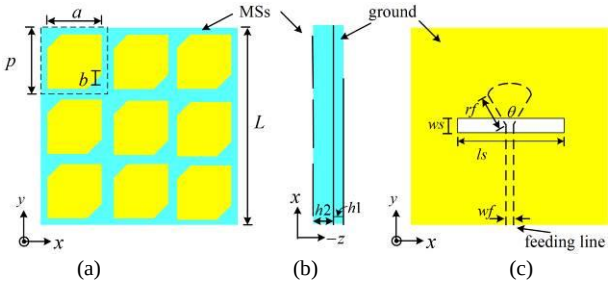

Fig. 2. Configuration of the element antenna

To understand the mechanism of CP radiation, an equivalent circuit model of two adjacent MS unit cells is provided in Fig. 3 [22]. When an LP EM wave is radiating from the slot, which is along the +y direction for this design, the EM field can be decomposed into two orthogonal components along diagonal directions (i.e., $\vec{E}_1$ and $\vec{E}_2$). Due to the truncated corners of the square patch, the inductance ($L_i(i=1,2)$) and capacitance ($C_i(i=1,2)$) are different and correspond to different equivalent impedance ($Z_i(i=1,2)$) values. When these two impedances satisfy $|Z_1|=|Z_2|$ and $|\angle Z_1-\angle Z_2|=90°$, CP radiation is achieved.

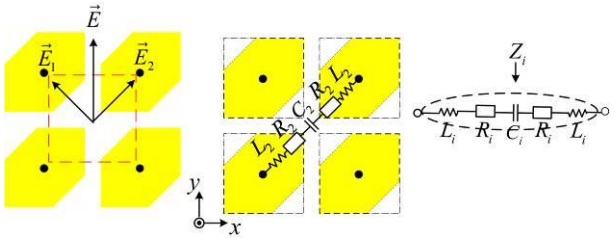

Fig. 3. Equivalent circuit model

Figs. 4(a) and (b) show the return loss (S11), axial ratio (AR), and gain of the element antenna. The simulated $|S11|\le -10$ dB is from 4.5 to

7.0 GHz. The 3-dB AR bandwidth is 5.55-5.85 GHz with an in-band gain variation from 6.20 dBi to 6.70 dBi. Fig. 4(c) gives the radiation patterns at 5.7GHz. The cross-polarization levels are below -17.5 dB in both the *xoz*- and *yoz*-plane.

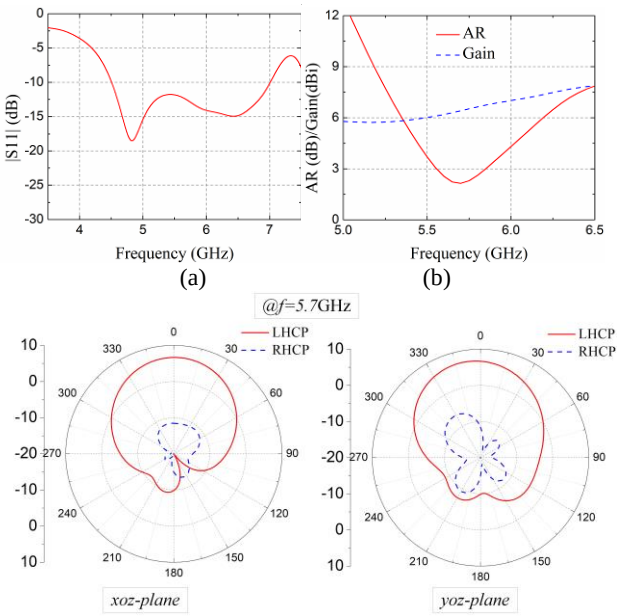

Fig. 4. Element antenna (a) S11, (b) AR, gain (c) radiation pattern at 5.7 GHz

The optimization goal is the maximization of the array's bandwidth covering most of the C-band subject to a maximum in-band AR lower than or equal to 3 dB. The critical design parameters and their search ranges are given in Table I. After a day (wall clock time) of optimization on a workstation with an Intel 8-core i9-9900K 3.6 GHz CPU, 64 GB RAM, and 8 GB NVIDIA Quadro RTX 4000 GPU, PSADEA obtains the design in Table I using 315 EM simulations. Figs. 5(b) and (c) shows the S11, AR, and gain of the PSADEA-optimized array. The PSADEA-optimized array yields a wide $|S11| \le -10$ dB bandwidth of 4-6.9 GHz and a 3-dB AR bandwidth of 4.2-7 GHz. Within the CP bandwidth of 4.2-6.9 GHz, the gain varies from 9.9 to 11.0 dBic. The peak gain of 11.5 dBic occurs at 6.35 GHz.

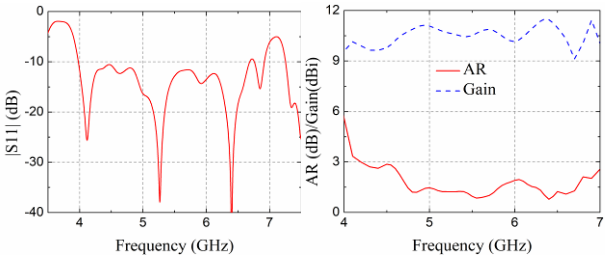

Fig. 5 Performance of the array (a)S11, (b)AR and gain

C. *Mechanism of broadband RCS reduction*

The broadband RCS reduction is achieved by the combination of two RCS reduction principles in the upper and lower operating frequency regions, in consonance with the explanations given in [18]. Different from the MSs used for CP bandwidth improvement in [18], the MS-based superstrate of each element antenna is used to convert the LP wave radiated from the LP slot antenna into CP radiation. To further clarify the mechanism, the equivalent schematic diagram extracted from the MS-based superstrate is depicted in Fig. 6. Two MS parts (Sections II and IV) and their adjacent grounded substrate parts (Sections I and III) can be viewed as a checkerboard reflecting screen. Sections II and IV are MSs consisting of 3×3 MS unit cells and their mirrored replica, respectively. Sections I and III are equal-sized substrate regions resting on metallic ground without a top metal covering.

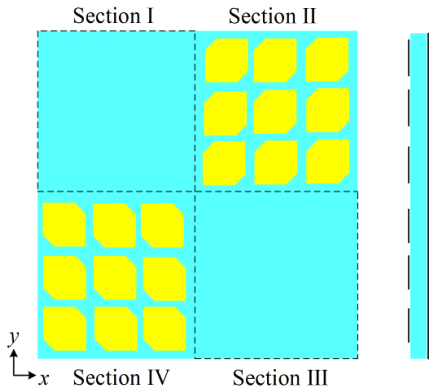

Fig. 6. Equivalent schematic diagram of the MS-based substrate

The mechanism of RCS reduction in the upper band is as follows. Fig. 7 shows the reflection magnitudes and phases of the MS and the grounded substrate unit cells. The simulations are carried out using the Master/Slave boundary in HFSS. According to Fig. 7(a), the reflection magnitudes of the MS and the grounded substrate are approximately equal in the frequency range of 8.0-16.0 GHz. As shown in Fig. 7(b), the phase difference ranges from 114.7° to 256° in this frequency band. The phase difference range of $180° \pm 37°$ is from 10.5-14.5 GHz, which can produce over 10 dB RCS reduction according to the phase cancellation principle [14].

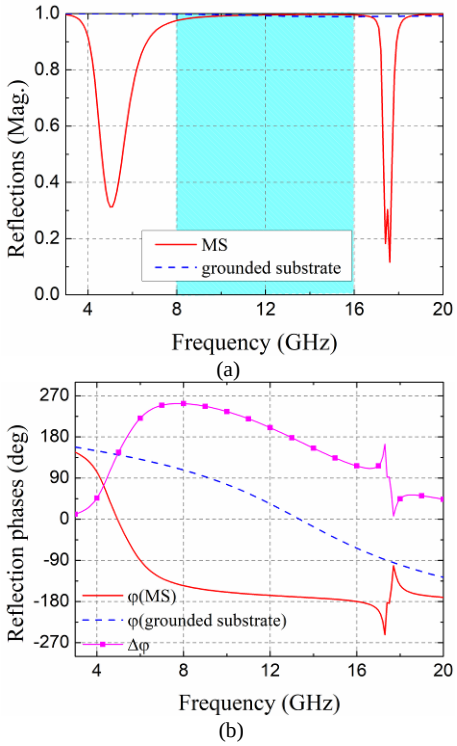

Fig. 7 (a) Reflection magnitudes and (b) reflection phases.

To study the mechanism of RCS reduction in the lower frequency region, an LP incident wave is considered as an example. The

co-polarization and cross-polarization components of the reflected wave are shown in Fig. 8. The co-polarization reflection coefficient (in dB) is less than -10 dB from 4.52 to 6.17 GHz. A narrow polarization conversion band is obtained in the higher frequency region. This indicates that most of the incident field is rotated in the cross-polarized direction. Taking a *y*-polarized incident wave as an example, the reflected fields in Sections II and IV are in anti-phase. Indeed, due to the polarization conversion property of the metasurfaces, for a *y*-polarized incident wave, the main energy is converted into its cross-polarized component (*x*-polarization), and the cross-components of the electromagnetic waves reflected by the MSs in Section II and the mirrored replica in Section IV are canceled out. Only the co-polarized components remain. Therefore, the total RCS is reduced in the lower operating frequency band according to the principle [17].

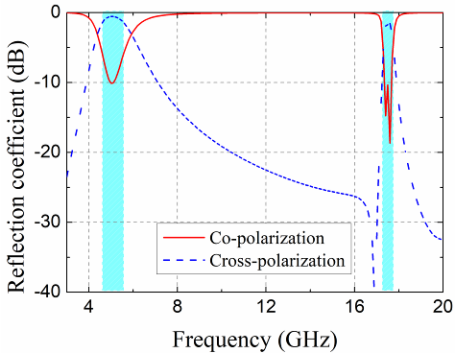

Fig. 8 Reflection coefficients in the low band

III. Measurements and Discussion

A prototype was fabricated and measured to validate the simulation results, see Fig. 9. The overall size of the array is 90.0 mm × 90.0 mm × 3.5 mm. The array is fed by an 50Ω SMA connector.

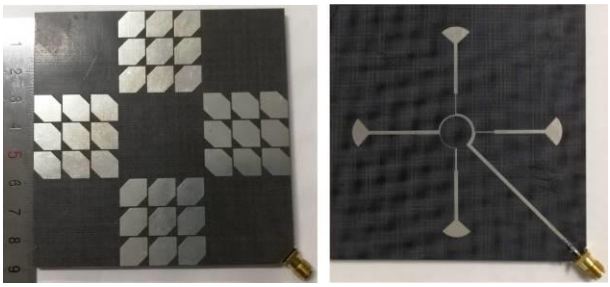

(a) (b)

Fig. 9 Fabricated prototype (a) front view, (b) back view.

The measured results are shown in Figs. 10. The measured $|S11| \le -10$ dB bandwidth and 3-dB AR bandwidth are in good agreement with the simulated ones. Fig. 11 gives the radiation patterns at 5.5GHz. The cross-polarization levels are below -20 dB in both the *xoz*- and *yoz*-plane. The main beam tilts are around 12° in both planes, which are attributed to the tilting of the radiation pattern of the element antenna and the introduction of phase shifts in the current distribution due to the staggered arrangement. The small discrepancies and ripples can be attributed to the typical causes: small fabrication and measurement errors, the glue between the upper and lower substrates, and the non-uniformity of the dielectric constant of the substrate.

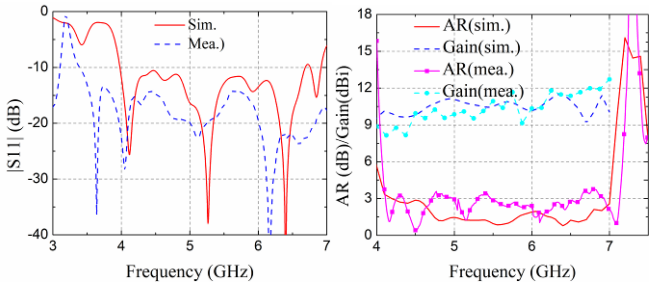

(a) (b)

Fig. 10 (a) Reflection coefficient (b) AR and gain.

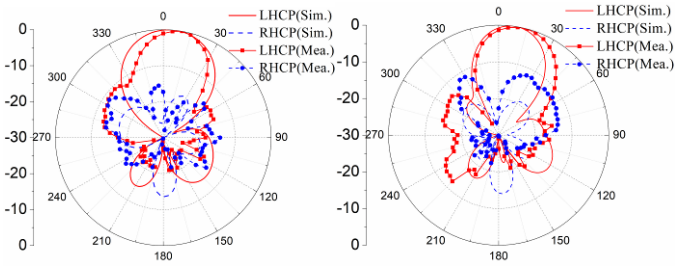

(a) (b)

Fig. 11 Normalized radiation patterns at 5.5 GHz (a) *xoz*-plane, (b) *yoz*-plane

The measured RCS reduction characteristic of the proposed array compared with the array without MS-based superstrate is shown in Fig. 12. It can be seen that the simulated RCS reduction (>0 dB) is obtained from 3 to 20 GHz for both *x*- and *y*-polarized normal incident plane waves (147.8%). The RCS reduction is over 5 dB in the band of 5-17.5 GHz (111.1%). Two minimum values occur at 5 GHz and 13.5 GHz, which correspond to the polarization conversion and 180° phase difference bands analyzed in Figs. 7 and 8, respectively. The scattering performance was measured in an anechoic chamber. Two horn antennas were used as transmitter and receiver, respectively. The array was placed in the far-field region. The performance in the band of 8-18 GHz was measured by using two types of horn antennas working in the bands 8-12 GHz and 12-18 GHz, respectively. The measured results are in good agreement with the respective simulation results, except for a small frequency shift. Figs. 13 and 14 show the monostatic RCS under different incident angles at the two frequencies in the low and high bands, respectively. An over 0 dB RCS reduction can be obtained within ±15° at 5 GHz and ±6° at 13.5 GHz. The narrower angles at the high frequency are reasonable according to array theory analysis [7].

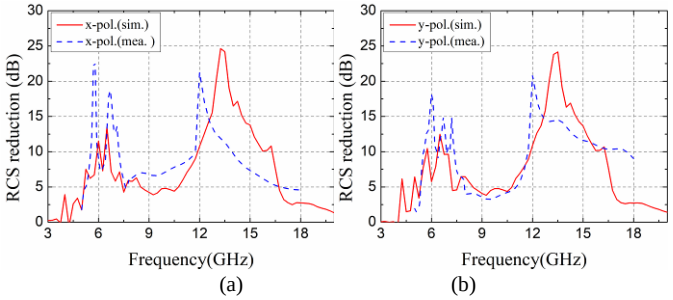

(a) (b)

Fig.12 Measured and simulated RCS reduction of the proposed array under (a) *x*-polarized and (b) *y*-polarized incident waves

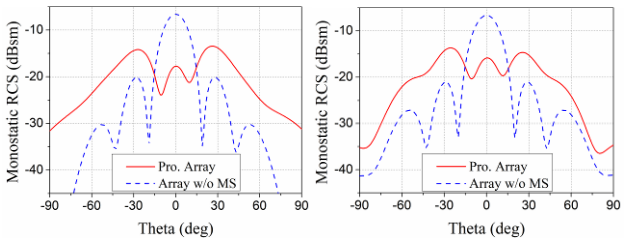

Fig. 13 Monostatic RCS at 5 GHz under (a) x-polarized and (b) y-polarized incident waves

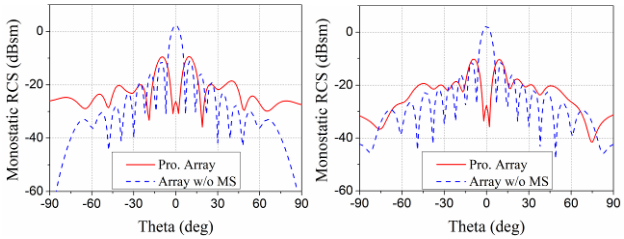

Fig. 14 Monostatic RCS at 13.5 GHz under (a) x-polarized and (b) y-polarized incident waves

The radiation and scattering performance of the proposed design is compared with the literature in Table I. For low RCS CP antennas, compared with [12], [18],[19], and [20], the proposed antenna yields by far the widest 3-dB AR bandwidth (50% relative bandwidth) using a state-of-the-art AI-driven antenna design optimization algorithm, and this is reached with a low profile and a small number of MS unit cells. Compared with the low-profile low-RCS LP slot antenna [10] and arrays in [16][17], the proposed antenna yields a wider over 5 dB RCS reduction band of 5-17.5 GHz (111.1%) with fewer MS cells.

TABLE II
COMPARSION WITH LOW-RCS METAMATERIAL-BASED ANTENNAS IN LITERATURE

Refs	Impedance bandwidth (GHz, %)	Polarization state/3-dB CP BW (GHz, %)	Peak gain (dBi)	RCS reduction BW in GHz and % (BW criterion)	Structure/Size(λ_0^3)
[10]	5.4-5.8 /7.1%	LP	9.5	4.35-7.8 GHz /56.8%(>6dB)	Slot antenna with AMCs (136 cells) $2.24\times2.24\times0.056$@5.6GHz (ε_{r1}=2.65)
[12]	26.7-37.2 /24.6%	CP/26.8-33.1 (21%)	20	28-48 GHz /52% (>0 dB)	F-P antenna with FSS-based superstrate (64 cells) $4.9\times4.9\times0.7357$@30GHz (ε_{r1}=6.15,ε_{r2}=2.2)
[13]	>8-12 />100%	CP/9-12 (20%)	15	>9-12 GHz />26%(>0dB)	F-P antenna with FSS-based superstrate (100 cells) $3.5\times3.5\times0.592$@10GHz (ε_{r1}=9.5,ε_{r2}=2.65)
[16]	4.45-4.75 /6.52%	LP	13.5	6-18 GHz /100% (>5 dB)	Slot antenna array with PCMs (100 cells) $0.92\times0.92\times0.061$@4.6GHz (ε_{r1}=4.4)
[17]	4.8-7.0 /37.3%	CP/5-6.27 (22.5%)	13	4.7-5.8 GHz /21.0%(>6dB)	Slot antenna with EBGs (64 cells) $1.81\times1.81\times0.05$@5.5GHz (ε_{r1}=3.5)
[18]	5.25-6.35 /19.0%	CP/5.27-6.18 (15.9%)	7.42	4.95-15.7 GHz /104.25%(>6dB)	Patch antenna with MSs (36 cells) $1.546\times1.546\times0.057$@5.5GHz (ε_{r1}=4.4)
[19]	~7.6-8.8 /14.63%	CP/~8.0-8.46 (~5.6%)	13	7.55-20.75 GHz /93.25% (>6 dB)	Patch antenna with PCMs (60 cells) $2.18\times2.18\times0.082$@8.2GHz (ε_r=2.65)
[20]	8.25-9.5 /14.08%	CP/8.25-9.5 (14.08%)	11.2	6-14 GHz /80% (>0 dB)	F-P antenna with PCM-based superstrate (100 cells) $1.8\times1.8\times0.45$@9GHz (ε_r=3.5)
This Work	4.0-6.9 /53.2%	CP/4.2-7.0 (50%)	11.5	5-17.5GHz /111.1% (>5 dB)	Slot antenna array with MSs (36 cells)

	$1.68\times1.68\times0.065$@5.6GHz
	(ε_r=3.5)

IV. Conclusion

A novel MS-inspired low-profile low-RCS CP slot array has been proposed in this work. The proposed array uses the sequential-rotation technique and a hybrid RCS reduction mechanism. The broadband RCS reduction is obtained based on two different destructive interference principles of a checkerboard structure in combination with an MSs and a grounded substrate. The polarization conversion property of the MS and the PSADEA-optimized sequentially rotated feeding network ensure a wide CP operating bandwidth. Measured and simulated results are in very good agreement. The low-profile design may find promising applications in aircraft and stealth platforms.

References

[1] E. F. Knott, J. F. Shaeffer, and M. T. Tuley, *Radar Cross Section*. Raleigh, NC, USA: SciTech, 2004.

[2] T. Liu, *et al.*, "RCS reduction of waveguide slot antenna with metamaterial absorber", *IEEE. Trans. Antennas Propag.*, vol. 61, no. 3, pp. 1479-1484, Mar. 2012

[3] S. Genovesi, F. Costa, and A. Monorchio, "Low-profile array with reduced radar cross section by using hybrid frequency selective surfaces," *IEEE Trans. Antennas Propag.*, vol. 60, no. 5, pp. 2327–2335, May 2012.

[4] Y. Zheng, *et al.*, "Wideband gain enhancement and RCS reduction of Fabry–Pérot resonator antenna with chessboard arranged metamaterial superstrate", *IEEE Trans. Antennas Propag.*, vol. 66, no. 2, pp. 590-599, Feb. 2018.

[5] Y. Han, *et al.*, "Novel low-RCS circularly-polarized antenna arrays via frequency selective absorber", *IEEE. Trans. Antennas Propag.* vol. 68, no. 1, Jan. 2020.

[6] Y. Li, *et al.*, "RCS reduction of ridged waveguide slot antenna array using EBG radar absorbing material", *IEEE Antennas Wireless Propag. Lett.*, vol. 7, pp. 473–476, June. 2008.

[7] J. C. I. Galarregui, et al., "Broadband radar cross-section reduction using AMC technology", *IEEE Trans. Antennas Propag.*, vol. 61, no. 12, pp. 6136-6143, Dec. 2013.

[8] W. Chen, C. A. Balanis, and C. R. Birtcher, "Checkerboard EBG surfaces for wideband radar cross section reduction", *IEEE Trans. Antennas Propag.*, vol. 63, no. 6, pp. 2636-2645, Mar. 2015.

[9] Y. Jia, *et al.*, "Broadband polarization rotation reflective surfaces and their applications to RCS reduction", *IEEE Trans. Antennas Propag.*, vol. 64, no. 1, pp. 179-188, Jan. 2016.

[10] Y. Zhao, *et al.*, "Broadband low-RCS metasurface and its application on antenna", *IEEE Trans. Antennas Propag.*, vol. 64, no. 7, pp. 2954-2962, July. 2016.

[11] L. Cong et al., "Ultra-wideband low-RCS circularly-polarized metasurface-based array antenna using tightly-coupled anisotropic element". *IEEE Access*, vol. 6, pp. 41738-41744, Jul. 2018.

[12] S. Zarbakhsh, *et al.*, "Broadband and high-gain circularly-polarized antenna with low RCS", *IEEE Trans. Antennas Propag.*, vol. 67, no. 1, pp.16-23, Jan. 2019.

[13] S. Zarbakhsh, *et al.*, "Optically transparent subarray antenna based on solar panel for CubeSat application", *IEEE Trans. Antennas Propag.*, vol. 68, no. 1, pp. 319-328, Jan. 2020

[14] L. Jidi, et al. "X-band and circularly polarized antenna with inborn RCS reduction." *IEEE Antennas Wireless Propag. Lett.*, vol. 17, no.8, pp. 1501-1504, Aug. 2018

[15] M. Guo, et al. "Circularly polarised antenna with low RCS using chessboard grid hollow substrate." *Elect. Lett., vol.* 55, no. 24 pp. 1265-1267, Nov. 2019.

[16] W. Zhang, Y. Liu and Y. Jia, "Circularly polarized antenna array with low RCS using metasurface-inspired antenna units," *IEEE Antennas Wireless Propag. Lett.*, vol. 18, no. 7, pp. 1453-1457, July. 2019.

[17] Q. Zheng, *et al.*, "Low-profile circularly polarized array with gain enhancement and RCS reduction using polarization conversion EBG structures", *IEEE Trans. Antennas Propag.* vol. 63, no. 8, pp. 2440-2445, Mar. 2020.

[18] Q. Zheng, et al., "A broadband low-RCS metasurface for CP patch antennas", *IEEE Trans. Antennas Propag.*, vol. 69, no. 6, pp. 3529-3534, June 2021

[19] Z. Liu, Y. Liu, and S. Gong, "Gain enhanced circularly polarized antenna with RCS reduction based on metasurface," IEEE Access, vol. 6, pp. 46856–46862, Aug. 2018

[20] K. Li, *et al.*, "A circularly polarized high-gain antenna with low RCS over a wideband using chessboard polarization conversion metasurfaces", *IEEE Trans. Antennas Propag.*, vol. 65, no. 8, pp. 4288-4292, Aug. 2017.

[21] H. Evans, *et al*., "Application of simulated annealing to design of serial feed sequentially rotated 2×2 antenna array," *Electron. Lett*, vol. 36, no. 24, pp. 1987–1988, Nov. 2000.

[22] H. L. Zhu, S. W. Cheung, X. H. Liu, and T. I. Yuk, "Design of polarization reconfigurable antenna using metasurface," *IEEE Trans. Antennas Propag.*, vol. 62, no. 6, pp. 2891–2898, Jun. 2014.

[23] B. Liu, *et al.*, "Efficient global optimisation of microwave antennas based on a parallel surrogate model assisted evolutionary algorithm," *IET Microw. Antennas & Propag.*, vol. 13, no. 2, pp. 149-155, Feb. 2019.

[24] M. O. Akinsolu, *et al*., "A parallel surrogate model assisted evolutionary algorithm for electromagnetic design optimization," *IEEE Trans. Emerg. Topics Comput. Intell.*, vol. 3, no. 2, pp. 93-105, Apr. 2019.

[25] B. Liu, *et al*., "An efficient method for antenna design optimization based on evolutionary computation and machine learning techniques," *IEEE Trans. Antennas Propag.*, vol. 62, no. 1, pp. 7-18, Jan. 2014.

[26] B. Liu, S. Koziel, and N. Ali, "SADEA-II: A generalized method for efficient global optimization of antenna design," *J. Comput. Design Eng.*, vol. 4, no. 2, pp. 86-97, Apr. 2017

[27] B. Liu, *et al.*, "An efficient method for complex antenna design based on a self adaptive surrogate model assisted optimization technique", *IEEE Trans. Antennas Propag.*, vol. 69, no. 4, pp. 2302-2315, April 2021.

[28] Q. Hua, *et al.*, "A novel compact quadruple-band indoor base station antenna for 2G/3G/4G/5G systems," *IEEE Access*, vol. 7, pp. 151350-151358, Oct. 2019.

[29] J. Zhang, *et al.*, "Automatic AI-driven design of mutual coupling reducing topologies for frequency reconfigurable antenna arrays", *IEEE Trans. Antennas Propag.*, vol. 69, no. 3, pp. 1831-1836, March 2021.

.